# Reduction of the Relative Intensity Noise of Broadband Sources Using Dual Fiber Ring Resonator

Yishi Liu, Jingjing Su, Xiaowan Luo, and Xingfan Chen

***Abstract*—Interferometric fiber-optic gyroscopes (IFOGs) are widely utilized due to their compact size and solid-state design. However, their sensitivity of detecting rotation is limited by the relative intensity noise (RIN) associated with the broadband source. To overcome this limitation, a conventional fiber ring resonator (FRR) can be employed to filter the RIN specifically at the IFOG frequency. Nonetheless, implementing this solution necessitates a fiber delay line with a length equal to that of the fiber coil. To address this challenge, we propose the utilization of passive and active dual FRRs and examine their RIN suppression characteristics. By utilizing the active dual FRR as an optimized gain point filter, we achieve a theoretical RIN suppression ratio equivalent to that of the traditional FRR, while significantly reducing the required length of the fiber delay line.**

***Index Terms*—Gyroscopes, optical fiber applications, optical fiber sensors.**

## NOMENCLATURE

| | |
|---|---|
| $c$ | speed of light in vacuum. |
| $n$ | index of fiber. |
| $f$ | electronic frequency. |
| $f_1$ | frequency at RIN suppression ratio $M_1$. |
| $G_i$ | gain. |
| $G_{i\mathrm{b}}$ | optimal gain points of active D-FRR. |
| $k_i$ | coupling ratios of OC. |
| $l_i$ | length of fiber. |
| $L_{\mathrm{D\text{-}FRR}}$ | total length of fiber segment in D-FRR. |
| $m$ | fiber savings ratio, $f_1 = m$·FSR/2. |
| $M_i$ | RIN suppression ratio. |
| $P$ | average power of source. |
| $p$,$q$ | $p$ and $q$ are co-prime numbers, and $p$: $q = l_1 : l_2$. |
| $RIN(f)$ | relative intensity noise before the optical spectral filter. |
| $RIN'(f)$ | relative intensity noise after the optical spectral filter. |
| $S(\upsilon)$ | optical spectrum. |
| $S'(\upsilon)$ | output optical spectrum. |
| $T_{\mathrm{RIN}}(f)$ | RIN response. |
| $T_{\mathrm{S}}(\upsilon)$ | optical spectral transmission. |
| $T_{\mathrm{P}}$ | light power response. |
| $\alpha_{ci}$ | coupler excess loss of OC. |
| $\alpha_{fi}$ | loss of fiber. |
| $\alpha_{\mathrm{NL1}}$ | equivalent net losses of m-FRR. |
| $\alpha_{\mathrm{NL2}}$ | equivalent net losses of s-FRR. |
| $\alpha_{\mathrm{NLt}}$ | total net loss of D-FRR. |
| $\upsilon$ | optical frequency. |

Manuscript received 13 July 2023; accepted 14 July 2023. Date of publication 17 July 2023; date of current version 26 July 2023. This work was supported in part by the National Natural Science Foundation of China under Grant 62075193, in part by the Zhejiang Provincial Natural Science Foundation of China under Grant LD22F050002, in part by the Major Scientific Project of Zhejiang Laboratory under Grant 2019MB0AD01, in part by the Ten Thousand Talents Program of Zhejiang Province under Grant 2017r51010. *(Yishi Liu and Jingjing Su contributed equally to this work.) (Corresponding author: Xingfan Chen.)*

Yishi Liu, Jingjing Su, and Xiaowan Luo are with the College of Optical Science and Engineering, Zhejiang University, Hangzhou 310058, China (e-mail: 12130004@zju.edu.cn; sujj@zju.edu.cn; 22130026@zju.edu.cn).

Xingfan Chen is with the College of Optical Science and Engineering, Zhejiang University, Hangzhou 310058, China, and also with the Quantum Sensing Center, Zhejiang Lab, Hangzhou 310000, China (e-mail: mycotty@zju.edu.cn).

Digital Object Identifier 10.1109/JPHOT.2023.3296161

## I. INTRODUCTION

HIGH-PRECISION interferometric fiber-optic gyroscopes (IFOGs) offer several advantages, including all-solid-state construction, high reliability, extended service life, and outstanding measurement sensitivity [1], [2], [3]. Consequently, they are well suited for long-term inertial navigation in applications such as intercontinental ballistic missile guidance, geophysical scientific research, and space exploration [4], [5], [6], [7]. Among the core components of IFOGs, broadband sources are crucial for determining the overall performance of the device. The performance of the light source directly affects the precision, stability, and accuracy of the IFOGs. Therefore, improving the performance of broadband light sources is a crucial factor for the development and enhancement of IFOGs.

A broadband light source can produce coherence lengths at the micrometer level, enabling the effective elimination of parasitic interference errors caused by backscattering in IFOGs [1]. However, the use of a broadband light source introduces relative intensity noise (RIN), which reduces the sensitivity of the device when performing high-precision measurements of angular velocity in IFOGs [8].

Various electronic methods have been used for RIN suppression. Overmodulation, for instance, involves using a modulated phase approximately equal to $\pi$ (instead of $\pi/2$) in IFOG to reduce noise. Killian et al. [9] used two photodetectors to detect the optical power and determined the time difference between light intensity fluctuations to counteract RIN. Optical methods have

also been proposed to suppress RIN. Hakimi et al. [10] and Suo et al. [11] proposed the reshaping of the optical spectrum using the saturated nonlinear gain of semiconductor optical amplifiers to increase the 3 dB linewidth. Guattari et al. [12] and Zheng et al. [13] used a specific phase-reduction structure comprising a polarization-preserving coupler and an isolator to reduce the noise power at the eigenfrequency of the IFOG. Zheng et al. [14] added a Faraday rotator mirror after the coupler to suppress RIN. Zheng et al. [15] used an unbalanced Mach-Zehnder interferometer between the amplified spontaneous emission (ASE) and the coupler to minimize RIN for filtering the optical spectrum based on the relationship between the two.

In recent years, a method was developed to suppress the RIN using a fiber ring resonator (FRR) as an optical spectral filter [16]. This technique involves filtering the optical spectrum through an FRR and suppressing RIN via the manipulation of the relationship between the RIN and the optical spectrum. Experimental results have demonstrated RIN suppression exceeding 20 dB [17]. However, this technique requires an optical fiber delay line of the same length as that of the coil of IFOG.

To overcome this disadvantage, this study proposed a new method, referred to as dual FRR (D-FRR for RIN suppression. Compared with the traditional FRR (T-FRR), this approach significantly reduces the required length of the optical fiber delay line used in the FRR. Further, the simulation results indicate that this method maintains the potential for effective RIN suppression without compromising performance. By selecting appropriate device parameters, D-FRR can achieve the same level of RIN suppression as T-FRR.

## II. D-FRR Principle

### A. Principle of RIN Suppression

The intensity noise of optical interferometric is categorized into three main types: RIN caused by the source, noise caused by photon scattering, and thermal noise caused by the detector, which are proportional to $P^1$, $P^{1/2}$, and $P^0$, respectively ($P$ is the optical power of the photoelectric detectors). When the optical power of the light source is sufficient to reach tens of microwatts, the RIN becomes the main noise source. Consequently, the RIN can occupy more than 90% of the total noise, especially in IFOGs. Therefore, RIN suppression of the broadband light source is particularly important in applications.

RIN is closely related to the optical spectrum. Let $S(\upsilon)$ be the optical spectrum and $\upsilon$ be the optical frequency. The power spectral density of the RIN at electronic frequency $f$ in broadband sources RIN($f$) can be expressed as follows [15], [18]:

$$RIN\left(f\right)=\int_0^{\infty}\frac{S\left(\upsilon\right)S\left(\upsilon+f\right)}{P^2}\mathrm{d}\upsilon, \tag{1}$$

where $P=\int_0^{\infty}S(\upsilon)\mathrm{d}\upsilon$ is the average power of the source.

When the optical spectral transmission $T_{\mathrm{S}}(\upsilon)$ is applied as an optical spectral filter to $S(\upsilon)$, the output optical spectrum $S'(\upsilon)$ can be represented as follows:

$$S'\left(\upsilon\right)=T_{\mathrm{S}}\left(\upsilon\right)S\left(\upsilon\right), \tag{2}$$

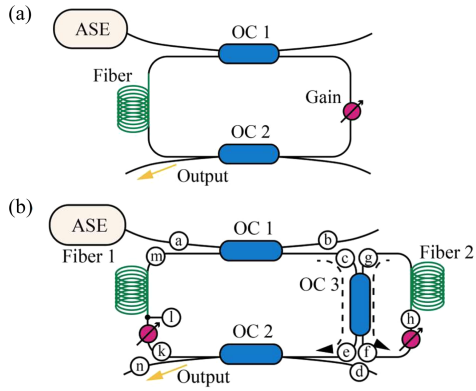


Fig. 1. (a) Configuration of the T-FRR. (b) Configuration of the D-FRR (OC: 2×2 optical coupler).

The RIN response $T_{\mathrm{RIN}}(\nu)$ can be expressed using (1) as follows [19]:

$$T_{\mathrm{RIN}}\left(f\right)=\frac{\int_{FSR}T_{\mathrm{S}}\left(f+\upsilon\right)T_{\mathrm{S}}\left(\upsilon\right)\mathrm{d}\upsilon}{FSR\cdot T_{\mathrm{P}}^2}, \tag{3}$$

where $T_{\mathrm{P}}=\int_{FSR}T_{\mathrm{S}}(\upsilon)\mathrm{d}\upsilon$ denotes the light power response of the optical spectral filter, and FSR represents the free spectral range of FRR. The relationship between RIN after the optical spectral filter, *RIN*'($f$), and RIN before the optical spectral filter, *RIN*($f$), can be described as

$$RIN'\left(f\right)=T_{\mathrm{RIN}}\left(f\right)RIN\left(f\right). \tag{4}$$

Thus, $T_{\mathrm{RIN}}(f)$ also represents the RIN suppression ratio of the optical spectral filter at electronic frequency $f$. The periodicity of both $T_{\mathrm{S}}(\nu)$ and $T_{\mathrm{RIN}}(f)$ are determined by the FSR, when the FSR is much smaller than the linewidth of the source [16].

### B. D-FRR Configuration

T-FRR, as shown in Fig. 1(a), has been established as an effective method for RIN suppression using a long fiber delay line. The term "Gain" refers to optical gain modules such as erbium-doped fiber amplifiers or semiconductor optical amplifiers. We introduced a D-FRR RIN suppression architecture, as illustrated in Fig. 1(b). The main FRR (m-FRR) was formed via the resonator with nodes c -> d -> e-> l -> m-> c. The resonator with nodes f -> h -> g -> f is referred to as the secondary FRR (s-FRR). ASE was inputted through port a and transported to port c from optical coupler (OC) 1. After propagation through Gain 1, the light propagated through the system and was split into two beams by OC 3. These beams were then directed to ports e and f. The beam at port e was further transmitted through the m-FRR. The beam at port f was transported through Gain 2 and fiber 2 and was then re-transmitted into OC 3 to produce a resonance. Further, the light passing through port e was split into two beams using OC 2. One beam was outputted through port n, and the other passed through Fiber 1 and converged with the ASE to produce another resonance. The D-FRR operates as a passive D-FRR when Gains ($G$) 1 and 2 are both less than or equal to zero. When $G_1$ or $G_2$ is less than zero, the D-FRR can be considered as an attenuator rather than as an amplifier.

TABLE I
PARAMETERS, THEIR SYMBOLS, AND STANDARD VALUES OF OPTICAL DEVICES IN A D-FRR

| Name | Para. | Symbols | Standard values |
|---|---|---|---|
| **Loss Para.** | Coupler excess loss of OC $i$ ($i$ = 1,2,3) | $\alpha_{ci}$ | 0.3 dB |
| | Loss of fiber $i$ ($i$ = 1,2) | $\alpha_{fi}$ | 0.2 dB/km |
| **Function Para.** | Coupling ratios of OC $i$ ($i$ = 1,2,3) | $k_i$ | - |
| | Length of fiber $i$ ($i$ = 1,2) | $l_i$ | - |
| | Gain $i$ ($i$ = 1,2) | $G_i$ | - |

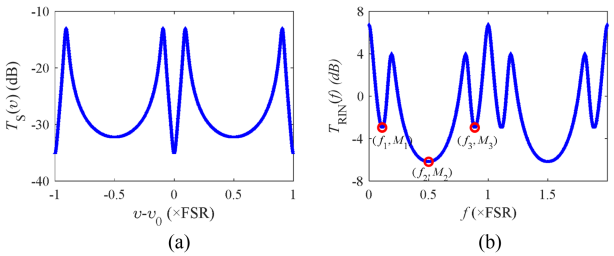


Fig. 2. (a) Optical spectral transmission and (b) RIN response of D-FRR. The negative gain corresponds to suppression. For these simulation results, $l_1 = l_2 = 500$ m, $k_1 = k_2 = 0.05$, $k_3 = 0.3$, $\alpha_c = 0.3$ dB, and $\alpha_f = 0.2$ dB/km.

Conversely, when Gains 1 and 2 are non-zero, it functions as an active D-FRR. The response of RIN suppression for passive and active D-FRRs is discussed in Sections III and IV, respectively.

The parameters of the optical devices used in the D-FRR are listed in Table I.

The loss parameter in optical systems indicates the amount of signal loss that occurs in different optical components. Although these loss parameters are not fixed and can vary between different components, in the case of the most commonly used components, the values are typically close to the standard values. Consequently, we employed the standard values of the loss parameter. Moreover, $T_S(\upsilon)$ and $T_{RIN}(\nu)$ of the D-FRR can be affected by different functional parameters. Therefore, various functional parameters were used in the analysis to examine the results.

The D-FRR filtered the optical spectrum based on the principle of the optical amplitude, which remained constant at the same position as the photoelectric field vector in a stable resonant state. Further information regarding the calculation of optical spectral responses can be found in Appendix A. A set of device parameter results is presented herein visually; the analysis of these results is presented in Sections III and IV. The functional parameters $l_1 = l_2 = 500$ m, $k_1 = k_2 = 0.05$, $k_3 = 0.3$, $T_S(\upsilon)$, and $T_{RIN}(\nu)$ are shown in Fig. 2(a) and (b).

As shown in Fig. 2, for the D-FRR, three minima of RIN suppression points existed within the FSR: ($f_1$, $M_1$), ($f_2$, $M_2$), and ($f_3$, $M_3$). Because of the symmetry of the optical spectral and RIN responses, $f_1 + f_3 = FSR$, $f_2 = FSR/2$, and $M_1 = M_3$. Further, $FSR = 2c/(n{\cdot}L)$ for the set of device parameters. For

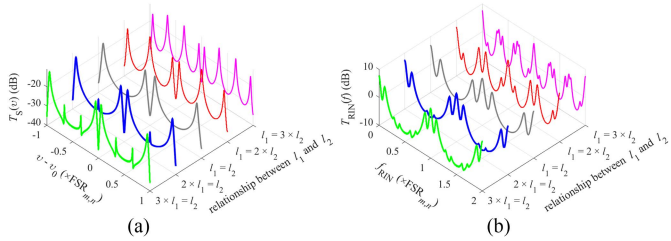


Fig. 3. (a) Optical spectral transmission and (b) RIN response of passive D-FRR at different $l_1$ and $l_2$ values. For these simulation results, $L_{D\text{-}FRR} = 1000$ m, $k_1 = k_2 = 0.05$, $k_3 = 0.3$, $\alpha_c = 0.3$ dB, and $\alpha_f = 0.2$ dB/km. The green, blue, dark gray, red, and pink lines show the $3l_1 = l_2$, $2l_1 = l_2$, $l_1 = l_2$, $l_1 = 2l_2$, and $l_1 = 3l_2$, respectively.

clarity in the presentation and subsequent discussion, we define $f_1$ as $m{\cdot}FSR/2$. In this case, $f_3$ can be expressed as $(2 - m){\cdot}FSR/2$.

For the optical interferometer represented by the IFOG, the signal to be measured was typically converted to have an appropriate frequency via modulation. Consequently, the measured signal was obtained via demodulation at that frequency. The signal must only yield a low noise around the modulation frequency $f_m$.

When the modulation frequency of the interferometer is at the proper frequency $f_m$, the working point of RIN suppression must be at this frequency. Consequently, when a T-FRR is used, the required equation is $f_m = (FSR_{T\text{-}FRR})/2$, where $FSR_{T\text{-}FRR}$ is the FSR of T-FRR and is equal to $c/(2n{\cdot}l)$. Thus, the fiber length is $L_{T\text{-}FRR} = c/(2n{\cdot}f_m)$.

When using D-FRR, $f_1 = (m{\cdot}FSR_{1:1})/2$, where $l_1 = l_2$, $l_1{:}l_2 = 1{:}1$, $FSR_{1:1}$ is $2c/(n{\cdot}L_{D\text{-}FRR})$, where the total length $L_{D\text{-}FRR} = l_1 + l_2$. The required equation is $f_m = (m{\cdot}FSR_{1:1})/2$. Thus, the fiber length $L_{D\text{-}FRR} = m{\cdot}c/(2n{\cdot}f_m)$. Consequently, when $m < 1$, the length of the fiber used in the FRR was reduced. The lower the value of $m$, the lower the amount of fiber used.

## III. PASSIVE D-FRR USING RIN REDUCTION

### A. Responses Depending on $l_1$–$l_2$ Relationship

First, we consider passive D-FRR, for which $G_1 = G_2 = 0$.

Section II-B presents an example of RIN suppression corresponding to the same fiber lengths of fibers 1 and 2. In this section, we examine the RIN relationships for different fiber delay line lengths for fibers 1 and 2.

When the lengths of the two FRRs differ, the output of the D-FRR exhibits significant variance, resulting in $T_{RIN}(f)$ that is obtained through (3). As shown in Fig. 3, there were $2(p+q)+1$ minimum RIN values within the FSR. However, owing to changes in the length ratio, the FSR also changed accordingly. If we represent the FSR as $FSR_{p,q}$ when the fiber delay line lengths are in the ratio $l_1{:}l_2 = p{:}q$, where $p$ and $q$ are co-prime numbers, then $FSR_{p,q} = (p + q)c/(n{\cdot}L_{D\text{-}FRR})$. For example, $FSR_{3,1}$ is twice the size of $FSR_{1,1}$. If $m_{3,1}FSR_{3,1} = m_{1,1}FSR_{1,1} = f_m$, then $m_{3,1}/m_{1,1} = 0.5$ is required when using the same fiber length in the FRR as in Section II-B. This necessitates precise control over the value of $m$ to reduce the fiber length, which complicates the process. Additionally, the $T_{RIN}(f)$ slope is steeper, thus indicating that $f_1$ becomes

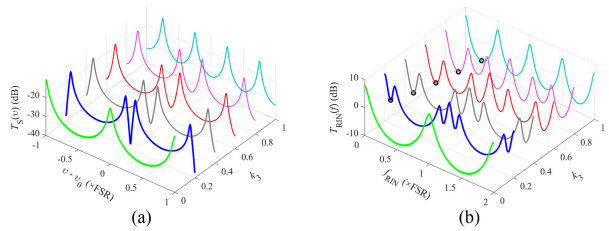


Fig. 4. (a) Optical spectral transmission and (b) RIN response of passive D-FRR. The negative gain corresponds to suppression. For these simulation results, $l_1 = l_2 = 500$ m, $k_1 = k_2 = 0.05$, $\alpha_c = 0.3$ dB, $\alpha_f = 0.2$ dB/km, and $k_3$ ranged as 0–1 in 0.2 intervals, which is shown by the green, blue, dark gray, red, pink, and light blue lines. The black circles show the $f_1$ and $M_1$ as a function of $k_3$.

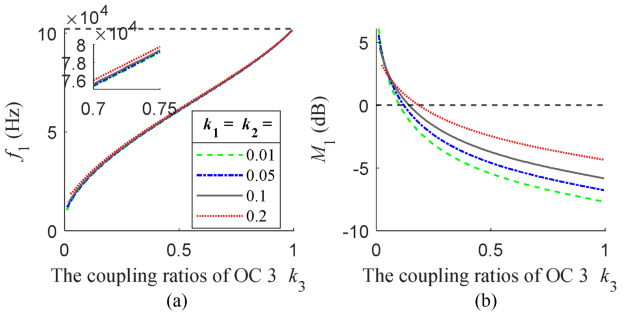


Fig. 5. (a) Relationship between frequency of RIN suppression ratio $f_1$ and different coupler ratios of OC 3. (b) Relationship between RIN suppression ratio $M_1$ and different coupler ratios of OC 3. Four different coupler ratios of OC 1 and OC 2 are chosen. The blue, orange, yellow, and violet lines show the coupler ratios of OC 1 and OC 2 corresponding to 0.01, 0.05, 0.1, and 0.2, respectively. The black-dashed lines in (a) and (b) show the RIN suppression frequency of the T-FRR and the cut-offs of RIN suppression, respectively.

unstable. Consequently, ideal RIN suppression parameters are achieved when the fiber lengths are equal, and the subsequent discussion is based on $l_1 = l_2$.

### B. Responses Depend on Coupling Ratio of OC

The three couplers OC 1, OC 2, and OC 3 have different effects in D-FRR. For a resonator, the net loss is closely related to the optical spectral transmission. The coupler ratios of OC 1 and OC 2 ($k_1$ and $k_2$) only affect the loss of the m-FRR but have no effect on the loss of the s-FRR, whereas OC 3 exchanges energy between the m-FRR and s-FRR.

First, we consider the effects of OC3. We consider $k_1 = k_2 = 0.05$ for passive D-FRR and the two fiber lengths as $l_1 = l_2 = 500$ m. The output response of the optical spectral transmission and RIN response for $k_1 = k_2 = 0.05$ and $k_3$ with values in the range of 0–1 at 0.2 intervals are shown in Fig. 4(a) and (b).

When $k_3$ is increased, the RIN suppression effect improves, albeit with an increase in $f_1$ (or $m$) in the passive D-FRR, as shown by the black circles in Fig. 4(b). The analysis in Section II-B shows that for the corresponding frequency, the required fiber length also increases, thus offsetting the advantage of using a passive D-FRR. This presents a tradeoff when a passive D-FRR is used, wherein a reduction in fiber delay line length and RIN suppression cannot be simultaneously achieved. However, this problem can be resolved in active D-FRR, as described in Section IV.

Next, we consider OC 1 and OC 2. When $k_1 = k_2$ ( = 0.01, 0.05, 0.1, or 0.2), and $k_3$ is in the range of 0–1, the frequency response of RIN suppression ratio $f_1$ and RIN suppression ratio $M_1$ of different $k_1$ and $k_2$ can be obtained with the same $k_3$. The results are shown in Fig. 5.

When $k_1$ and $k_2$ are increased, the net loss within the m-FRR increases, whereas the net loss in the s-FRR remains unaltered, resulting in an inferior RIN suppression effect, as shown in Fig. 5. Because $k_1$ and $k_2$ correspond to m-FRR loss changes, this observation implies that offset losses can enhance RIN suppression, while ensuring that $f_1$ remains small. Thus, using an active D-FRR as an optical spectrum filter is better than using a passive D-FRR.

## IV. Active D-FRR Using RIN Reduction

### A. Possible Range of Coordinates ($G_1$, $G_2$)

In each steady resonator, the condition of no net gain must be satisfied because the light power cannot increase continuously regardless of the position of the FRR. To ensure stability, gains 1 and 2 in the FRR must satisfy the aforementioned requirements and be limited to a set of interrelated maximum values.

Assuming no energy exchange between the two resonators, the equivalent net losses of m-FRR ($\alpha_{\mathrm{NL1}}$) and s-FRR ($\alpha_{\mathrm{NL2}}$) can be expressed by (5) and (6), respectively.

$$\alpha_{NL1} = 3\alpha_c + \alpha_f l_1 + 10\lg(1-k_2) + 10\lg(1-k_1) + 10\lg(1-k_3) + G_1 \quad (5)$$

$$\alpha_{NL2} = \alpha_f l_2 + \alpha_c + 10\lg(1-k_3) + G_2 \quad (6)$$

According to the analysis, $\alpha_{\mathrm{NL1}} \leq 0$ and $\alpha_{\mathrm{NL2}} \leq 0$ because the FRR should be in a steady-state condition.

Owing to energy exchanges between m-FRR and s-FRR, the analysis presented above only provides a maximum limit for the gain. Although the net loss of its FRR varies with $G_1$ and $G_2$, the mutual constraint between $G_1$ and $G_2$ must be analyzed. Because the analysis process is complex, a detailed analysis is presented in Appendix B. The total net loss ($\alpha_{\mathrm{NLt}}$) in the D-FRR can be expressed as

$$\alpha_{\mathrm{NLt}} = 2\alpha_c + \alpha_{\mathrm{de}} + \alpha_f l_1 + 10\lg(1-k_1) + 10\lg(1-k_2) + G_1, \quad (7)$$

where $\alpha^*_{\mathrm{de}} = \frac{1-\alpha_c^*(\alpha_f l_2+G_2)^*+2\alpha_c^*(\alpha_f l_2+G_2)^* k_3-k_3}{1-\alpha_c^*(\alpha_f l_2+G_2)^*+\alpha_c^*(\alpha_f l_2+G_2)^* k_3}\alpha_c^*$ expre-sses the actual loss from nodes d to e. To simplify the expression, the $^*$ operation symbol is included in the formula. For $\alpha$ and $\alpha^*$ satisfy the conversion relationship $\alpha^* = 10\log_{10}(\alpha)$, where the unit of $\alpha$ is dB, whereas $\alpha^*$ is a unitless quantity.

For a set of coupler ratios $k_1$, $k_2$, and $k_3$, the $G_1$ and $G_2$ values must simultaneously satisfy three inequalities: $\alpha_{\mathrm{NLt}} \leq 0$, $\alpha_{\mathrm{NL1}} \leq 0$, and $\alpha_{\mathrm{NL2}} \leq 0$. The possible range of gains for the parameters described in Section II-B is shown in Fig. 6.

In Fig. 6, the blue region represents the possible range in which ($G_1$, $G_2$) is located. Further, $\alpha_{\mathrm{NLt}} \leq 0$ is more restrictive on the coordinates ($G_1$, $G_2$) than $\alpha_{\mathrm{NL1}} \leq 0$ and $\alpha_{\mathrm{NL2}} \leq 0$. Herein, two limit cases are analyzed. When $G_2$ tends to negative infinity, the loss of the s-FRR is infinite, and the s-FRR cannot transmit light power to the m-FRR. Herein, $\alpha_{\mathrm{NL1}} = \alpha_{\mathrm{NLt}}$. However, when $G_1$ tends to positive infinity, as in the previous analysis, we obtain

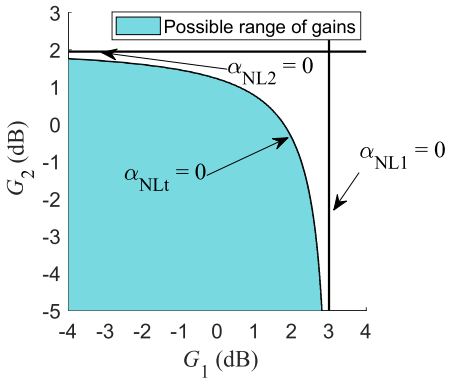


Fig. 6. Possible range between $G_1$ and $G_2$. For these simulation results, $l_1 = l_2 = 500$ m, $k_1 = k_2 = 0.05$, $k_3 = 0.3$, $\alpha_c = 0.3$ dB, and $\alpha_f = 0.2$ dB/km. The blue region shows the possible range in which ($G_1$, $G_2$) is located. When $G_1$ or $G_2$ is less than zero, it can be considered as an attenuator rather than an amplifier.

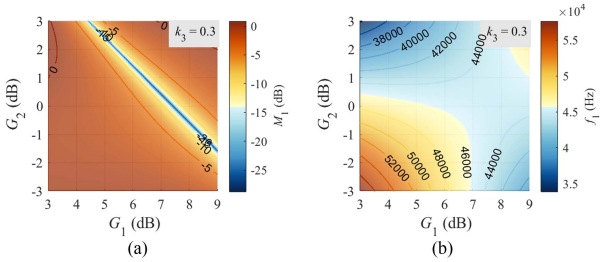


Fig. 7 (a) RIN suppression ratio $M_1$ and (b) frequency $f_1$ at RIN suppression ratio $M_1$ for $k_3 = 0.3$.

$\alpha_{NL2} = \alpha_{NLt}$. The proof in Appendix B shows that the two cases presented above are included when $\alpha_{NLt} \leq 0$.

### B. Responses Depending on $G_1$ and $G_2$

This section discusses the effects of $G_1$ and $G_2$ on the D-FRR. As demonstrated in Section III-B, when the loss decreases, the proportion of its RIN suppression gradually increases. In addition, as demonstrated in Section III-C, $G_1$, and $G_2$ must satisfy the $\alpha_{NL1} \leq 0$, $\alpha_{NL2} \leq 0$, $\alpha_{NLt} \leq 0$; therefore, this section discusses the RIN suppression parameters ($f_1$ and $M_1$) for different $k_3$ values under this inequality constraint.

Let $l_1 = l_2 = 500$ m, $k_1 = k_2 = 0.5$, $\alpha_c = 0.3$ dB, and $\alpha_f = 0.2$ dB/km. The RIN suppression ratio $M_1$ and frequency at the RIN suppression ratio $f_1$ are shown in Fig. 7.

A straight line representing $M_1$ tends towards negative infinity corresponding to the best RIN suppression ratio as shown in Figs. 7(a). Theoretically, the actual RIN suppression on these lines tends to infinity, or the RIN tends to zero (minus infinity in dB). However, owing to the simulation inaccuracy, a small offset exists in the RIN. Moreover, not all points at this straight line can satisfy the steady-state resonator condition. The coordinates ($G_1$, $G_2$) must be constrained using (3). Considering Fig. 7(a) as an example and combining it with Fig. 3, the only possible cross point of this line and the possible range of ($G_1$, $G_2$) are obtained as shown in Fig. 8(a).

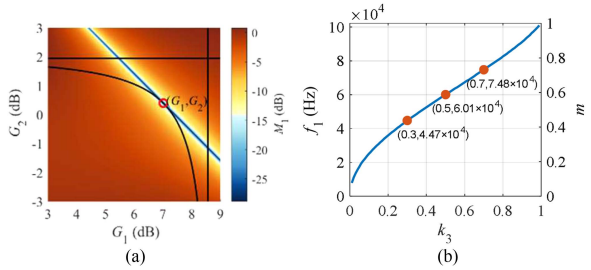


Fig. 8. (a) Black line represents the boundary condition for ($G_1$, $G_2$), and the thermodynamic diagram is the same as that in Fig. 7(a). (b) $f_1$ and $m$ vs. $k_3$.

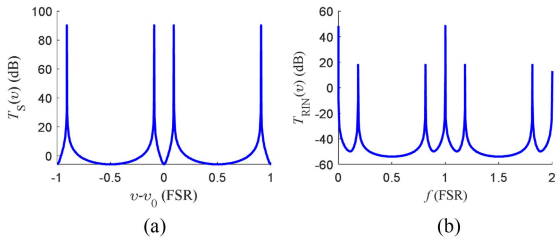


Fig. 9. (a) Optical spectral transmission and (b) RIN response of D-FRR the negative gain corresponds to suppression. For the simulation, the following values were set: $l_1 = l_2 = 500$ m, $k_1 = k_2 = 0.5$, $k_3 = 0.3$, $G_1 = 7.0206$, $G_2 = 0.4$.

The optimal gain point is achieved as follows:

$$G_{1b} = -3\alpha_c - \alpha_f l_1 - 10\lg(1-k_1) - 10\lg(1-k_2), \quad (8)$$

$$G_{2b} = -\alpha_c - \alpha_f l_2, \quad (9)$$

where $G_{1b}$ and $G_{2b}$ are the optimal gain points of the active D-FRR.

The $G_{1b}$ and $G_{2b}$ correspond to the total loss of the m-FRR and s-FRR without the loss of the coupler ratio $k_3$ (the derivation is provided in Appendix C). In the parameters shown in Fig. 7, the coordinates ($G_{1b}$, $G_{2b}$) correspond to (7.0206, 0.4), which meet the requirements of the boundary range at $\alpha_{NLt} = 0$. Moreover, we observed that by adopting the optimal gain point ($G_{1b}$, $G_{2b}$) in an active D-FRR, the suppression of RIN $M_1$ can be approximated to infinity, which indicates that the RIN is close to zero.

If the parameters listed above are used, the optical spectral transmissions $T_S(\nu)$ and RIN response $T_{RIN}(\nu)$ are as shown in Fig. 9.

Here, $f_1 = 0.11\,\mathrm{FSR}_{1,1}$, $M_1 = -49.9$ dB, $f_2 = 0.5\,\mathrm{FSR}_{1,1}$, $M_2 = -53.9$ dB. The length of the fiber delay line is reduced to 22% of its value used in the T-FRR. In addition, RIN suppression in $M_1$ is similar to that in $M_2$, which provides a more intuitive explanation for the impact of the active D-FRR on resolving the tradeoff of the passive D-FRR. By further decreasing $k_3$, the length of the fiber delay line is shortened further, and the suppression of RIN is not weakened.

## V. Experiments

In this section, we present an example of a passive D-FRR to validate our model. The configuration of the D-FRR remains the same as shown in Fig. 1(a), with each fiber having a length

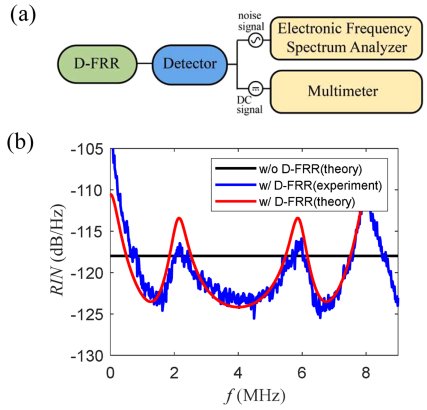


Fig. 10. (a) RIN analysis system used to measure RIN experimentally. (b) RIN response of D-FRR. For the simulation and experiment, the following values were set: $l_1 = l_2 = 25$ m, $k_1 = k_2 = 0.98$, $k_3 = 0.55$.

of 25 m. The coupler ratios of OC 1 and OC 2 are set to $k_1 = k_2 = 0.02$, while the coupler ratio of OC 3 is 0.55.

The setup of the RIN analysis system, which is used to measure RIN experimentally, is shown in Fig. 10(a). The power spectral density of the detector voltage of RIN, $S_V(f)$, is analyzed using an electronic spectrum analyzer. In addition, a multimeter measures the direct current (DC) signal of detected voltage $V$. The MFLI from Zurich Instrument and KEITHLEY 2010 were the electronic frequency spectrum analyzer and multimeter used to measure the noise and DC signals, respectively. Firstly, we used a multimeter to measure the bias voltage $V_0$ of the detector when there was no light input. We then connected the light source to the detector and measured the noise signal $S_V(f)$ and DC voltage $V$ using an electronic frequency spectrum analyzer and multimeter, respectively, when there was an optical input. The measured noise intensity (when MFLI was used) was less than 10 nV/rt-Hz, which was much smaller than the RIN.

In this case, the RIN is given by

$$RIN(f) = \frac{S_V(f)}{\overline{\Delta V}^2}, \tag{10}$$

where $\Delta V = V - V_0$ and $\overline{\Delta V}$ is the average $\Delta V$ over time.

The measured and simulated RIN at the output of the FRR are shown in Fig. 10(b). The simulation values for $f_1$ and $M_1$ are 1.368 MHz and $-5.826$ dB, respectively, while the experimental values are 1.478 MHz and $-4.97$ dB, respectively. The error arises from variations in ring length and insertion loss. Despite errors, the simulation accurately and reliably represents the RIN response.

Under these conditions, the T-FRR requires a 50 m fiber delay line, equivalent to the length of the fiber coil in the IFOG. In contrast, the D-FRR requires a fiber coil length of 138.3 m. Thus, a substantial saving of approximately 64% of the fiber delay line length is achieved.

## VI. Conclusion

We proposed the D-FRR as a novel approach and comprehensively investigated its optical spectral transmission and RIN responses. By utilizing the same fiber length in both the m-FRR and s-FRR, we observed three distinct minima within the FSR. We discussed both the passive and active D-FRR in detail.

We demonstrated that the use of a fiber delay line c in the passive D-FRR can be minimized by adjusting $k_3$, where smaller values of $k_3$ result in shorter delay coil lengths. However, the RIN suppression is inferior. In the active D-FRR, the use of a fiber delay line can also be minimized by adjusting $k_3$. Upon applying the gains $G_1$ and $G_2$ at optimal gain points $G_{1b}$ and $G_{2b}$, the RIN suppression tends towards infinity and the RIN tends to zero. Finally, a passive D-FRR experiment was conducted to demonstrate the reliability of our analysis.

The proposed approach effectively addresses the limitations of the traditional T-FRR, which typically requires the same fiber length as the sensing coil of the IFOG. Furthermore, our solution has the potential to revolutionize RIN suppression by enabling precise control of the loss in FRR and the coupling ratio of the coupler, resulting in a significant reduction in the required fiber length.

## Disclosure

The authors declare no conflicts of interest.

## Appendix A
## Derivation of Spectral Response

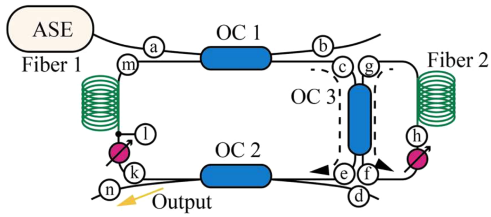


Fig. A1. Model of a dual fiber ring resonator with nodes.

The model of a dual ber ring resonator with nodes is shown as Fig. A1. The transmission relationships between the input and output ports of each OC are expressed as

$$\begin{bmatrix} E_b \\ E_c \end{bmatrix} = K_c(\alpha_{c1}, k_1) \begin{bmatrix} E_a \\ E_m \end{bmatrix}, \tag{A.1}$$

$$\begin{bmatrix} E_e \\ E_f \end{bmatrix} = K_c(\alpha_{c2}, k_2) \begin{bmatrix} E_d \\ E_g \end{bmatrix}, \tag{A.2}$$

$$\begin{bmatrix} E_n \\ E_l \end{bmatrix} = K_c(\alpha_{c3}, k_3) \begin{bmatrix} E_k \\ E_e \end{bmatrix}, \tag{A.3}$$

where [20], [21]

$$K_c(\alpha_c, k) = 10^{\frac{\alpha_c}{20}} \begin{bmatrix} \sqrt{1-k} & j\sqrt{k} \\ j\sqrt{k} & \sqrt{1-k} \end{bmatrix}. \tag{A.4}$$

Here, $\alpha_c$ is the excess loss of OCs and $k$ is the coupling ratio of the OC.

The transmission relationships between the input and output ports of optical fibers are expressed as

$$E_m = K_f(\alpha_{f1}, l_1) E_l, \tag{A.5}$$

$$E_{\mathrm{g}} = \mathrm{K_f}\left(\alpha_{\mathrm{f2}}, l_2\right) E_{\mathrm{h}}, \tag{A.6}$$

where

$$\mathrm{K_f}\left(\alpha_{\mathrm{f}}, l\right) = 10^{-\frac{\alpha_{\mathrm{f}} l}{20}} \exp\left(-j\beta l\right). \tag{A.7}$$

Here, $\beta = 2\pi\nu n/c$ is the transmission constant of light, $n$ is the refractive index of the optical fiber, $\alpha_{\mathrm{f}}$ is the loss of fiber, and $l$ is the length of the fiber.

The transmission relationships between the input and output ports of gains are

$$E_{\mathrm{d}} = \mathrm{K_l}\left(G_1\right) E_{\mathrm{c}}, \tag{A.8}$$

$$E_{\mathrm{h}} = \mathrm{K_l}\left(G_2\right) E_{\mathrm{f}}, \tag{A.9}$$

where

$$\mathrm{K_l}\left(G\right) = 10^{\frac{G(\mathrm{dB})}{20}} = G^*. \tag{A.10}$$

where $G$ is the gain coefficient; when $G > 0$ dB, G indicates the gain provided by the gain module; when $G < 0$ dB, G indicates the loss provided by the gain module, and when $G = 0$ dB, G indicates that the gain module has no effect. To simplify the expression, the operator symbol $^*$ is included in the formula. The unit of $G$ is dB, while $G^*$ is a unitless quantity. These parameters satisfy the conversion relationship $G^* = 10\log_{10}(G)$.

We define $a_{ij} = E_i/E_j$, which can be found in (A.1)–(A.6), where $a_{ij}$ is the amplitude transfer relationship from $i$ to $j$ ($i \neq j$). Further, $E_i$ and $E_j$ are the amplitudes at positions $i$ and $j$, respectively. Because the amplitudes of the electric field at the same position are the same after the FRR is stabilized [22], we can deduce the response of optical spectrum $T_{\mathrm{na}}(\nu)$ between nodes a and n as follows.

$$\begin{aligned} T_{\mathrm{na}}\left(\upsilon\right) &= \left|\frac{E_{\mathrm{n}}}{E_{\mathrm{a}}}\right|^2 \\ &= \left|\frac{a_{\mathrm{ne}}a_{\mathrm{ed}}a_{\mathrm{dc}}a_{\mathrm{ca}} + a_{\mathrm{ne}}a_{\mathrm{eg}}a_{\mathrm{gh}}(\upsilon)a_{\mathrm{hf}}a_{\mathrm{fd}}a_{\mathrm{dc}}a_{\mathrm{ca}}}{1 - a_{\mathrm{cm}}a_{\mathrm{ml}}(\upsilon)a_{\mathrm{le}}a_{\mathrm{ed}}a_{\mathrm{dc}} - a_{\mathrm{cm}}a_{\mathrm{ml}}(\upsilon)a_{\mathrm{le}}a_{\mathrm{eg}}a_{\mathrm{gh}}(\upsilon)a_{\mathrm{hf}}a_{\mathrm{fd}}a_{\mathrm{dc}}}\right|^2 \end{aligned} \tag{A.11}$$

## Appendix B
## Derivation of Total Net Loss $\alpha_{\mathrm{NLt}}$

We still use the method of optical amplitude to deduce $\alpha_{\mathrm{NLt}}$. First, the power transfer relationship between the couplers of the m-FRR and s-FRR is analyzed. The amplitude relationship between m-FRR and s-FRR can be expressed as

$$\begin{aligned} E_{\mathrm{e}} &= \sqrt{\alpha_{\mathrm{c}}^*}\left[\sqrt{1-k_3}E_{\mathrm{c}} + \sqrt{k_3}E_{\mathrm{g}}\right] \\ E_{\mathrm{f}} &= \sqrt{\alpha_{\mathrm{c}}^*}\left[\sqrt{k_3}E_{\mathrm{c}} + \sqrt{1-k_3}E_{\mathrm{g}}\right]. \end{aligned} \tag{B.1}$$

Consequently, the light power of nodes e and f can be expressed as

$$\begin{aligned} P_{\mathrm{e}} &= E_{\mathrm{e}}E_{\mathrm{e}}^* \\ &= \alpha_{\mathrm{c}}^*\left[\left(1-k_3\right)P_{\mathrm{d}} + k_3 P_{\mathrm{g}} + \sqrt{\left(1-k_3\right)k_3}\left(E_{\mathrm{d}}E_{\mathrm{g}}^* + E_{\mathrm{d}}^*E_{\mathrm{g}}\right)\right] \\ P_{\mathrm{f}} &= E_{\mathrm{f}}E_{\mathrm{f}}^* \\ &= \alpha_{\mathrm{c}}^*\left[k_3 P_{\mathrm{d}} + \left(1-k_3\right)P_{\mathrm{g}} + \sqrt{\left(1-k_3\right)k_3}\left(E_{\mathrm{d}}E_{\mathrm{g}}^* + E_{\mathrm{d}}^*E_{\mathrm{g}}\right)\right]. \end{aligned} \tag{B.2}$$

According to the method shown in Appendix A, we have

$$E_{\mathrm{g}} = \frac{a_{\mathrm{gh}}a_{\mathrm{hf}}\left(\upsilon\right)a_{\mathrm{fd}}}{1 - a_{\mathrm{gh}}a_{\mathrm{hf}}\left(\upsilon\right)a_{\mathrm{fg}}}E_{\mathrm{d}} = T_{\mathrm{gd}}\left(\upsilon\right)E_{\mathrm{d}}, \tag{B.3}$$

where

$$T_{\mathrm{gd}}\left(\nu\right) = \frac{i\sqrt{\alpha_{\mathrm{c}}^*k_3}}{\sqrt{\left(-G_2 - \alpha_{\mathrm{f}}L_2\right)^*}e^{i\beta(\nu)L_2} - \sqrt{\alpha_{\mathrm{c}}^*\left(1-k_3\right)}}. \tag{B.4}$$

Therefore, the amplitude cross product term can be expressed as

$$E_{\mathrm{d}}E_{\mathrm{g}}^* + E_{\mathrm{d}}^*E_{\mathrm{g}} = \left[T_{\mathrm{gd}}\left(\nu\right) + T_{\mathrm{gd}}(\nu)^*\right]P_{\mathrm{d}} = 2\mathrm{Re}\left(T_{\mathrm{gd}}\left(\nu\right)\right)P_{\mathrm{d}}. \tag{B.5}$$

Moreover,

$$\begin{aligned} &2\mathrm{Re}T\left(\upsilon\right) + 2\mathrm{Re}T\left(-\upsilon\right) \\ &= 2\mathrm{Re}\left(\frac{i\sqrt{\alpha_{\mathrm{c}}^*k_3}}{\sqrt{\left(-G_2-\alpha_{\mathrm{f}}L_2\right)^*}e^{i2\pi n\upsilon L_2/\mathrm{c}} - \sqrt{\alpha_{\mathrm{c}}^*\left(1-k_3\right)}}\right) \\ &\quad + 2\mathrm{Re}\left(\frac{i\sqrt{\alpha_{\mathrm{c}}^*k_3}}{\sqrt{\left(-G_2-\alpha_{\mathrm{f}}L_2\right)^*}e^{-i2\pi n\upsilon L_2/\mathrm{c}} - \sqrt{\alpha_{\mathrm{c}}^*\left(1-k_3\right)}}\right) \\ &= \frac{i\sqrt{\alpha_{\mathrm{c}}^*k_3}}{\sqrt{\left(-G_2-\alpha_{\mathrm{f}}L_2\right)^*}e^{i2\pi n\upsilon L_2/\mathrm{c}} - \sqrt{\alpha_{\mathrm{c}}^*\left(1-k_3\right)}} \\ &\quad + \frac{-i\sqrt{\alpha_{\mathrm{c}}^*k_3}}{\sqrt{\left(-G_2-\alpha_{\mathrm{f}}L_2\right)^*}e^{-i2\pi n\upsilon L_2/\mathrm{c}} - \sqrt{\alpha_{\mathrm{c}}^*\left(1-k_3\right)}} \\ &\quad + \frac{i\sqrt{\alpha_{\mathrm{c}}^*k_3}}{\sqrt{\left(-G_2-\alpha_{\mathrm{f}}L_2\right)^*}e^{-i2\pi n\upsilon L_2/\mathrm{c}} - \sqrt{\alpha_{\mathrm{c}}^*\left(1-k_3\right)}} \\ &\quad + \frac{-i\sqrt{\alpha_{\mathrm{c}}^*k_3}}{\sqrt{\left(-G_2-\alpha_{\mathrm{f}}L_2\right)^*}e^{i2\pi n\upsilon L_2/\mathrm{c}} - \sqrt{\alpha_{\mathrm{c}}^*\left(1-k_3\right)}} \\ &= 0. \end{aligned} \tag{B.6}$$

This term is an odd function centered on $v = FSR$; therefore, the integral in the FSR is zero. The equation listed above can be simplified to

$$\begin{aligned} P_{\mathrm{e}} &= \alpha_{\mathrm{c}}^*\left[\left(1-k_3\right)P_{\mathrm{d}} + k_3 P_{\mathrm{g}}\right] \\ P_{\mathrm{f}} &= \alpha_{\mathrm{c}}^*\left[k_3 P_{\mathrm{d}} + \left(1-k_3\right)P_{\mathrm{g}}\right] \end{aligned}. \tag{B.7}$$

Because node g and node f are associated based on the relationship

$$P_{\mathrm{g}} = \left(\alpha_{\mathrm{f}}l_2 + G_2\right)^* P_{\mathrm{f}}, \tag{B.8}$$

we obtain

$$\alpha_{\mathrm{de}}^* = \frac{P_{\mathrm{e}}}{P_{\mathrm{d}}} = \frac{1 - \alpha_{\mathrm{c}}^*\left(\alpha_{\mathrm{f}}l_2 + G_2\right)^* + 2\alpha_{\mathrm{c}}^*\left(\alpha_{\mathrm{f}}l_2 + G_2\right)^*k_3 - k_3}{1 - \alpha_{\mathrm{c}}^*\left(\alpha_E l_2 + G_2\right)^* + \alpha_{\mathrm{c}}^*\left(\alpha_{\mathrm{f}}l_2 + G_2\right)^*k_3}\alpha_{\mathrm{c}}^*. \tag{B.9}$$

Therefore, the net total loss coefficient in the D-FRR can be expressed as

$$\alpha_{\mathrm{NLt}} = 2\alpha_{\mathrm{c}} + \alpha_{\mathrm{de}} + \alpha_{\mathrm{f}}l_1 + 10\lg\left(1-k_1\right) + 10\lg\left(1-k_2\right) + G_1. \tag{B.10}$$

## APPENDIX C
## BEST RIN SUPPRESSION GAIN PARAMETER

Two methods, maximum gain, and equivalent resonator, were used to derive the gain parameter, which corresponded to the best RIN suppression.

### A. Maximum Gain

In a stable FRR, the maximum power relationship is allowed in the m-FRR and s-FRR when OC 3 introduces only insertion loss between nodes e and d or between nodes f and g. Further, there is no energy exchange between nodes d and f or between nodes e and g.

$$\begin{aligned} P_{\mathrm{e}} &= \alpha_{\mathrm{c}}^{*} P_{\mathrm{d}} \\ P_{\mathrm{f}} &= \alpha_{\mathrm{c}}^{*} P_{\mathrm{g}}, \end{aligned} \tag{C.1}$$

where $P_i$ represents the optical power at node $i$ in the resonant. The total net loss line is as shown in (B.10). Consequently, $\alpha_{\mathrm{de}}^{*} = \alpha_{\mathrm{c}}^{*}$,

$$\frac{1-\alpha_{\mathrm{c}}^{*}(\alpha_{\mathrm{f}} l_2 + G_2)^{*} + 2\alpha_{\mathrm{c}}^{*}(\alpha_{\mathrm{f}} l_2 + G_2)^{*} k_3 - k_3}{1-\alpha_{\mathrm{c}}^{*}(\alpha_E l_2 + G_2)^{*} + \alpha_{\mathrm{c}}^{*}(\alpha_{\mathrm{f}} l_2 + G_2)^{*} k_3} = 1. \tag{C.2}$$

The result for $G_2$ corresponds to the maximum RIN suppression. Equation (C.2) can be simplified as [22]

$$\alpha_{\mathrm{c}} + \alpha_{\mathrm{f}} l_2 + G_2 = 0. \tag{C.3}$$

The value of $G_1$ at maximum RIN suppression can be derived using $\alpha_{\mathrm{de}}^{*} = \alpha_{\mathrm{c}}^{*}$ and (7)

$$3\alpha_{\mathrm{c}} + \alpha_{\mathrm{f}} l_1 + 10\lg(1-k_1) + 10\lg(1-k_2) + G_1 = 0. \tag{C.4}$$

Thus, the best working point $(G_{1\mathrm{b}}, G_{2\mathrm{b}})$ is obtained as follows:

$$\begin{aligned} G_{1\mathrm{b}} &= -3\alpha_{\mathrm{c}} - \alpha_{\mathrm{f}} l_1 - 10\lg(1-k_1) - 10\lg(1-k_2) \\ G_{2\mathrm{b}} &= -\alpha_{\mathrm{c}} - \alpha_{\mathrm{f}} l_2. \end{aligned} \tag{C.5}$$

### B. Equivalence of m-FRR and s-FRR

First, we disregard the gain stability constraint (5)–(7) and assume that the best gain parameter $(G_{1\mathrm{b}}, G_{2\mathrm{b}})$ corresponds to the best RIN suppression. The slope of the best RIN suppression line formed by $(G_{1\mathrm{b}}, G_{2\mathrm{b}})$ is $k_{\mathrm{slope1}} = k$ $(k < 0)$.

The m-FRR and s-FRR can be reciprocally swapped because of the gain equivalent of the resonant. The RIN suppression ratio obtained at this time should be at the same point, with the best resonant RIN suppression line tangent point being the same as the previous analysis point, which is the same $(G_{1\mathrm{b}}, G_{2\mathrm{b}})$ point. Based on the m-FRR and s-FRR swap analysis, the slope of the best-resonant RIN suppression line as the maximum gain line should be $k_{\mathrm{slope2}} = 1/k$ at this time.

Because the two curves are the same, their slopes are equal, i.e., $k_{\mathrm{slope1}} = k_{\mathrm{slope2}}$, implying that $k = -1$. Therefore, the slope of the maximum gain point is the cross-point of the maximum gain line, and $\alpha_{\mathrm{NLt}} = 0$.

It can be proven that the result is the same as that shown in Appendix C-A.

## REFERENCES


[1] H. C. Lefevre, *The Fiber-Optic Gyroscope*. Norwood, MA, USA: Artech House, 2022.

[2] E. Udd and M. J. Digonnet, Eds., *Design and Development of Fiber Optic Gyroscopes*. Bellingham, WA, USA: SPIE, 2019, doi: 10.1117/3.2522293.

[3] D. He, Y. Wu, Y. Li, Z. Zhang, C. Peng, and Z. Li, "Stability improvement enabled by four-state modulation in dual-polarization fiber optic gyroscopes," *Opt. Commun.*, vol. 452, pp. 68–73, Dec. 2019, doi: 10.1016/j.optcom.2019.07.013.

[4] K. Shang, M. Lei, Q. Xiang, Y. Na, L. Zhang, and H. Yu, "Near-navigation-grade interferometric fiberoptic gyroscope with an integrated optical chip," *Chin. Opt. Lett.*, vol. 18, no. 12, Sep. 2020, Art. no. 120601, doi: 10.3788/COL202018.120601.

[5] S. Blin, M. Bishop, K. Parameswaran, M. J. Digonnet, and G. S. Kino, "Pickup suppression in Sagnac-based fiber-optic acoustic sensor array," *Proc. SPIE*, vol. 6004, pp. 46–56, 2005, doi: 10.1117/12.633773.

[6] Y. Cao, D. He, D. Zhang, W. Zhang, L. Li, and Z. Li, "High sensitivity interferometric fiber optic gyroscopes for 6-component seismograph," in *Proc. Opt. Fiber Sensors Conf.*, 2020, Paper W3.6, doi: 10.1364/OFS.2020.W3.6.

[7] J. Mou, J. Su, L. Miao, and T. Huang, "Research on field application technology of dynamic angle measurement based on fiber optic gyroscope and autocollimator," *IEEE Sensors J.*, vol. 21, no. 13, pp. 15308–15317, Jul. 2021, doi: 10.1109/JSEN.2021.3072641.

[8] P. R. Morkel et al., "Noise characteristics of high-power doped-fibre superluminescent sources," *Electron. Lett.*, vol. 26, no. 2, pp. 96–98, 1990, doi: 10.1049/el:19900066.

[9] K. M. Killian, M. Burmenko, and W. Hollinger, "High-performance fiber optic gyroscope with noise reduction," *Proc. SPIE*, vol. 2292, pp. 255–263, Nov. 1994, doi: 10.1117/12.191838.

[10] F. Hakimi and J. D. Moores, "RIN-suppressed ultralow noise interferometric fiber optic gyroscopes (IFOGs) for improving inertial stabilization of space telescopes," *Proc. SPIE*, vol. 8610, pp. 63–70, Mar. 2013, doi: 10.1117/12.2009246.

[11] X. Suo et al., "Ultralow-noise broadband source for interferometric fiber optic gyroscopesemploying a semiconductor optical amplifier," *Appl. Opt.*, vol. 60, no. 11, pp. 3103–3107, Apr. 2021, doi: 10.1364/AO.419969.

[12] F. Guattari et al., "Touching the limit of FOG angular random walk: Challenges and applications," in *Proc. DGON Intertial Sensors Syst.*, 2016, pp. 1–13, doi: 10.1109/InertialSensors.2016.7745662.

[13] Y. Zheng, C. Zhang, L. Li, L. Song, and Y. Zhang, "All-optical relative intensity noise suppression method for the high precision fiber optic gyroscope," *Proc. SPIE*, vol. 10158, pp. 149–157, 2016, doi: 10.1117/12.2246725.

[14] Y. Zheng, H. Xu, J. Song, L. Li, and C. Zhang, "Excess relative-intensity-noise reduction in a fiber optic gyroscope using a Faraday rotator mirror," *J. Lightw. Technol.*, vol. 38, no. 24, pp. 6939–6947, Dec. 2020, doi: 10.1109/JLT.2020.3020432.

[15] Y. Zheng, C. Zhang, and L. Li, "Influences of optical-spectrum errors on excess relative intensity noise in a fiber-optic gyroscope," *Opt. Commun.*, vol. 410, pp. 504–513, 2018, doi: 10.1016/j.optcom.2017.10.037.

[16] H. Zhang, X. Chen, X. Shu, and C. Liu, "Angular random walk improvement of a fiber-optic gyroscope using an active fiber ring resonator," *Opt. Lett.*, vol. 44, no. 7, pp. 1793–1796, Apr. 2019, doi: 10.1364/OL.44.001793.

[17] Y. Liu, X. Luo, and X. Chen, "Improvement of angle random walk of fiber-optic gyroscope using polarization-maintaining fiber ring resonator," *Opt. Exp.*, vol. 30, no. 17, pp. 29900–29906, Aug. 2022, doi: 10.1364/OE.462109.

[18] J. W. Goodman, *Statistical Optics*. Hoboken, NJ, USA: Wiley, 2015.

[19] H. Zhang, X. Chen, X. Shu, and C. Liu, "Fiber optic gyroscope noise reduction with fiber ring resonator," *Appl. Opt.*, vol. 57, no. 25, pp. 7391–7397, Sep. 2018, doi: 10.1364/AO.57.007391.

[20] G. P. Agrawal, *Fiber-Optic Communication Systems* (Wiley Series in Microwave and Optical Engineering), 5th ed. Hoboken, NJ, USA: Wiley, 2022.

[21] R. A. Chipman, G. Young, and W. S. T. Lam, *Polarized Light and Optical Systems* (Optical Sciences and Applications of Light). Boca Raton, FL, USA: CRC Press, 2018.

[22] I. S. Amiri and A. Afroozeh, *Ring Resonator Systems to Perform Optical Communication Enhancement Using Soliton*. Berlin, Germany: Springer, 2014.